ARTICLE

Unveiling the Oxidation Behavior of a Binary Mg–Y Alloy

Jie Li[1] | Haoyu Wang[1] | Fang Yi[2] | Yonghao Gao[1] | Chuming Liu[1]

[1]School of Materials Science and Engineering, Central South University, Changsha, China | [2]Hunan Xiangya Stomatological Hospital, Central South University, Changsha, China

Correspondence: Yonghao Gao (gaoyonghao_009@163.com)

Received: 14 October 2024 | **Revised:** 17 November 2024 | **Accepted:** 2 December 2024

Funding: The study was supported by the Natural Science Foundation of Hunan Province (2023JJ30673).

Keywords: isothermal oxidation | Mg–Y alloy | XPS analysis | Y_2O_3 scale

ABSTRACT

Magnesium and its alloys are the most promising lightweight metallic materials because of their outstanding mechanical performance. However, Mg alloys have long been criticized for their low oxidation resistance. In this study, the isothermal oxidation of a Mg–Y alloy at 350°C was investigated, and the resulting oxide scale was systematically characterized using an optical microscope, scanning electron microscope (SEM), X-ray diffraction (XRD), X-ray photoelectron spectroscopy (XPS), and other analytical techniques. The findings reveal that isothermal oxidation results in (i) an increase in the average Y content along grain boundaries, from 1.41 to 3.05 at.%, and surface enrichment of Y content from 0.86 to 3.07 at.% after 6 to 48 h of oxidation; (ii) inhomogeneous oxidation caused by microstructural heterogeneity; and (iii) the formation of an oxide scale consisting of a mixture of MgO and oxygen-deficient Y_2O_3 at the oxide/substrate interface, driven by the inward transport of oxygen anions. The molar ratio of MgO to Y_2O_3 was found to vary with oxidation time.

1 | Introduction

The low density, high specific strength, and good mechanical properties of magnesium alloys have assured their wide popularity for industrial applications [1–5]. Nevertheless, Mg and its alloys have high chemical activities, and remarkable oxygen affinity in particular, making them readily oxidized in ambient air to form a MgO scale on the sample surface [6]. Even though it has been proven that the naturally formed MgO is normally compact enough to provide some extent of protection to the bulk metal, such oxidation might be dramatically accelerated, leading to a reduced MgO compactness as the temperature increases. Such deteriorated oxidation might induce various side effects associated with surface chemical alteration, surface degradation [7] as well as increased complexity while deforming magnesium-based alloys [8]. For example, it has been challenging to deform magnesium alloys due to the inactivity of the non-basal slip systems at ambient temperature; such a problem might be relieved by increasing the deformation temperature. Magnesium alloys are generally hot worked at 300°C–500°C depending on their chemical compositions. In such a temperature range, the occurrence of oxidation is inevitable, and methods for oxidation protection should be developed.

Two strategies involving surface engineering (like surface ion-doping) [9] and bulk additions of appropriate alloying elements [10–14] have been explored to enhance the oxidation resistance of magnesium alloys. The profound oxidation inhibition of the two methods relies on the ability to increase the compactness of the oxide layer. Even though ion doping has yielded many successes in retarding oxidization, such a method is still criticized due to the drawbacks associated with insufficient lifetime caused by the limited ion-penetration depth [15].

Alloying magnesium with appropriate elements such as Ca [16], Be [17], Nd [18], Ce [19], and Y [20–23], and so forth, might retard the oxidation process because either of the following two benefits: (i) these alloying elements help to form compact

metallic oxides other than the porous MgO (that usually formed on pure Mg) and (ii) the alloying elements are more active than Mg, and can provide the so-called reactive element effects (REEs) [1]. Wu et al. [24, 25] conducted a systematic investigation into the long-term oxidation behavior of rare-earth magnesium alloys at 500°C. By analyzing the oxidation mechanism from thermodynamic and kinetic perspectives, they found that the type and content of active elements play a crucial role in determining the formation of the oxide scale and the alloy's antioxidant properties. Among all the alloying elements, yttrium seems to be the most promising one because of its ability to provide the two benefits simultaneously. Theoretically, the addition of Y to Mg would facilitate the formation of Y_2O_3 apart from the single MgO layer because of the even higher oxygen affinity of Y [10, 20]. Moreover, the appreciably higher Pilling-Bedworth ratio of Y_2O_3 than that of MgO [20], that is, 1.13 *v.s.* 0.81 helps to enhance the compactness of the oxide layer, thus lowering the oxidation rate. Such theoretical hypothesis has been experimentally proven many times, and many successes regarding oxidation inhabitation of Mg by Y addition have been reported [20–23, 26]. Inspired by the existing success, ever-increasing attention has been devoted toward understanding the kinetics as well as the factors influencing the oxidation of the Y-containing magnesium alloys. For example, Yu et al. [22] observed that the oxidation resistance of Mg-xY alloys (x = 0.5, 1.0, 1.7, 3.7, and 5.5 wt.%) improved with increasing Y content at temperatures below their melting range (550°-625°C). This enhancement was attributed to the transformation of the oxide scales from a loose MgO layer to a dense Y_2O_3 layer, which prevents the direct contact of atmosphere O_2 to the underlying substrate, thereby reducing further oxidation. It has been well acknowledged that the oxidation rate increases monotonically with the temperature, while the Y concentration seems to parabolically affect the oxidation rate [10, 21]. The effects of temperature on the oxidation process are much more complex; both positive (due to the up-taking of oxygen to form oxide scale) and negative (due to the loss of surface physisorption moisture or the localized evaporation of Mg) weight gains of the Y-containing magnesium alloys have been reported.

It has to be admitted that the study on the oxidation process of the Y-containing Mg alloys is still not comprehensive. Almost all the existing studies start by monitoring the weight changes by thermogravimetric analysis (TGA) of the samples during the oxidation process. Then, the samples that experience significant weight changes are subjected to detailed microstructural analysis in an attempt to unveil their oxidation mechanisms. The dilemma of this strategy is that the weight changes cannot be detected until the oxidation temperature is high enough (> 500°C); therefore, the samples that oxidized at lower temperatures are normally overlooked. It should be emphasized that understanding the oxidation mechanism at < 400°C is of practical significance because the heat treatment and hot working of the Y-containing alloys are generally conducted in this temperature range. More importantly, this material, showing excellent mechanical thermal stability, is also expected to be used in the same temperature range.

Therefore, a binary Mg–Y alloy with a dilute concentration of Y was oxidized at 350°C for up to 500 h, and the oxidize scale evolution during the oxidation process was investigated systematically, based on which the growth kinetics of the oxide at this temperature was discussed.

2 | Materials and Methods

2.1 | Alloy Preparation

Commercially pure Mg and Mg-20 wt.% Y master alloy were melted under the protection of a gas mixture comprising CO_2 and SF_6 at around 750°C. The melt was thoroughly stirred by purging Argon to ensure its chemical homogeneity. Afterward, the melt was held at 750°C for more than 2 h to allow the settlement or floatation of the impurities. Then the melt was transported to a direct-chill casting unit to get an ingot with a diameter of 100 mm. The ingot was isothermally held at 525°C for 20 h for homogenization and then extruded at 450°C to get a final diameter of 18 mm.

The chemical composition of the sample was measured by an inductively coupled plasma emission spectrometer (ICP, SPECTRO BLUE SOP), and the results are tabulated in Table 1. It is clear that apart from Y, the alloy also contains a marginal impurity of Gd, Si, Mn, and Fe.

2.2 | High-Temperature Oxidation

The as-extruded alloy was cut to get samples with dimensions of $\Phi 18 \times 10$ mm for subsequent high-temperature oxidation. All samples were first ground using successively refining abrasive SiC papers (up to 3500 grit), then polished using silica suspension (0.04 μm), and finally cleaned with alcohol to obtain a clean mirror-like surface. The isothermal oxidation experiment was conducted in an electric furnace (TAISITE SX-4-10P) at 350°C in ambient air [25]. The samples were oxidized for up to 500 h, a significantly longer duration than typically reported in the existing literature [17, 21–23, 27, 28] due to the lower oxidation rate at the studied temperature. During this period, one sample was withdrawn from the furnace at designated intervals (6, 12, 24, 60, 200, 300, 400, and 500 h) for subsequent microstructural characterization.

2.3 | Microstructure Characterization

The surface morphologies of the oxidized samples were viewed using an optical microscope (Olympus BX51M) as well as a scanning electron microscope (SEM, TESCAN MAIA3). An energy dispersive X-ray spectrometer (EDS) attached to the SEM and an electron probe micro analyzer (EPMA, JXA-8230) were utilized for the chemical analysis. The oxidized sample surface was also characterized using an atomic force microscope (AFM, Bruker Dimension Icon) in the noncontact tapping mode. A lateral area of $30 \times 30\ \mu m^2$ was imaged under ambient conditions. A polynomial background was subtracted from the

TABLE 1 | Chemical composition of the studied Mg–Y alloy (at.%).

Element	Mg	Y	Gd	Si	Mn	Fe
at.%	*bal.*	0.53	0.04	0.02	0.01	0.005

acquired AFM image using the Gwyddion software to minimize the effects of artifacts on the reported height profiles.

The cross-sectional view of the oxide scale/metallic substrate was also characterized using a transmission electron microscope (TEM) to disclose the growth of the oxide scale. The oxidized samples were milled using a Gallium ion beam in a focused ion beam (FIB) system (TESCAN AMBER) to get the electron-transparent cross-sectional TEM samples. Such samples were then immediately transported to a field emission TEM system (Talos F200X S/TEM), where the bright field image, selected area electron diffraction pattern as well as chemical distribution was acquired.

The phase compositions of the samples were characterized using the X-ray diffraction (XRD) technique using a D/max 2550VB diffractometer with Cu Kα radiation ($\lambda = 0.1554$ nm). The diffractometer was operated at a work voltage of 40 kV and a current of 450 mA. The diffraction pattern was collected under the Bragg-Brentano geometry with the 2θ range of 10° to 85°, a step size of 0.02°, and a scanning rate of 6 deg min^{-1}. The phase compositions of the samples were determined following the conventional search/match procedure by referring to the standard powder diffraction files loaded in the MDI JADE 9.0 software.

The quantitative elemental and chemical state information of the uppermost layer of the samples oxidized at different times was acquired using X-ray photoelectron spectroscopy (XPS, Shimadzu AXIS SUPRA+). The XPS sputter depth profile along the oxide scale thickness of the sample oxidized for 60 h was collected using a PHI5000 VersaProbe III photoelectron spectrometer. While acquiring the depth profile, the sample surface was sputtered using an Ar^+ ion beam, and the XPS spectra were collected at a sputtering time interval of 3 min. The Ar^+ ions were emitted by applying a 4 kV-voltage biasing on the ion gun; the Ar^+ ion bombarded a surface area of 3×3 mm on the sample surface from the direction of 45° with respect to the sample normal. The etching rate of the metallic Mg–Y alloy covered with an oxide scale was hard to determine due to the lack of a reliable reference sample, even though the calibrated etching rate using the SiO/Si layer was well-defined to be 3.5 nm min^{-1}. Moreover, the chemical/structural inhomogeneity of the oxide-metal sample also means the etching rate might vary along the depth. Therefore, the sputtering time instead of depth was utilized in the present work to avoid any possible error induced by the inconsistent etching rate. Both of the two photoelectron spectrometers utilized the non-monochromatic Al Kα radiation (1486.6 eV) as the excitation source and operated with a chamber vacuum better than 7×10^{-1} Pa. The electron analyzer and lens are operated in the constant analyzer energy (CAE) mode. The XPS survey spectra, as well as the high-resolution C 1*s*, O 1*s*, Mg 1*s*, Mg 2*p,* and Y 3*d* spectra, were individually collected within their respective binding energy (BE) range. The spectra were analyzed using the CasaXPS software, and the characteristic BE of each core-orbital was referenced in the XPS Handbook and the NIST database. The BE scale of the XPS spectra was calibrated against the characteristic binding energy of C 1*s* following the procedure proposed by Greczynski et al. [29]. While deconvoluting the XPS spectra, the Shirley background was subtracted, and the peak area ratio as well as the BE difference of the Mg 2*p*- and Y 3*d*-orbital splitting doublets were strictly constrained.

3 | Results and Discussion

3.1 | Optical Microstructural Characterization

The optical images showing the surface morphologies of the samples after oxidation at various times are presented in Figure 1. It should be mentioned that all the images were acquired with the same optical microscope setting; therefore, it is rational to attribute the observed changes among the images to the surface variations of the oxidized samples. For comparison, the optical morphology of the alloy directly after polishing without oxidation was also viewed and exhibited in Figure 1a. It has been mentioned that the sample has been polished to a mirror-like finish; therefore, specular reflection occurs when the light of the optical microscope is directed on the sample surface. In this case, the sample does not present any visible grain boundaries other than the embedded secondary intermetallic particles. Although the alloy used in the present study only contains a dilute concentration of Y (the Y content here is far below its equilibrium solid solubility in Mg), it is still impossible to exclude the formation of these secondary phase particles because the casting and extrusion procedures utilized to prepare the alloy is far away from equilibrium condition. From the phase diagram of the Mg–Y binary system [30], it is believed that the particles may have a formula of $Mg_{24}Y_5$.

After oxidation at 350°C for 6 h, the original metallic luster of the mirror surface gradually disappeared. Instead, the sample surface was decorated with an ivory color (Figure 1b), based on which it is assumed that the oxidized scale may contain an appreciable amount of Y_2O_3 [31]. On the other hand, the yellowish surface is decorated with a network of lighter contrast. As compared with the grain boundary characters of the unoxidized sample, as reported in our previous research [32], it is clear that there is an obvious correlation between the network and the original grain boundaries of the substrate Mg–Y alloy. Even though these boundaries separate neither the grains of the substrate (i.e., well beneath the oxide scale, as will be explained later) nor the grains of the oxidize scales (i.e., generally several nanometers), they are still termed as grain boundaries in the context for convenience. From these findings, it may be speculated that the entire sample surface had been oxidized, but the oxidation that takes place along the original grain boundaries and at the grain interiors may have followed different kinetics.

Extending the oxidation further to 12 h, the color of the light-yellow sample surface became darker, indicating the thickening of the oxide scale. The boundaries of the decorating network became thicker. Furthermore, an obvious contrast variation can be observed (Figure 1c) that may be due to the inhomogeneous oxidation of the sample surface. Such oxidization inhomogeneity is possibly attributed to the difference in crystallographic orientations of the substrate Mg-Y alloy (that has been reported in Figure 1c of our previous publication [32]), as it has been proven many times that different crystal facets may yield different oxidation kinetics [33, 34].

When the oxidization time was doubled to 24 h (Figure 1d) and continuously prolonged up to 60 h (Figure 1e), the heterogeneous oxidation process still prevails, that is, the width of the network increases and the contrast variations from grain to

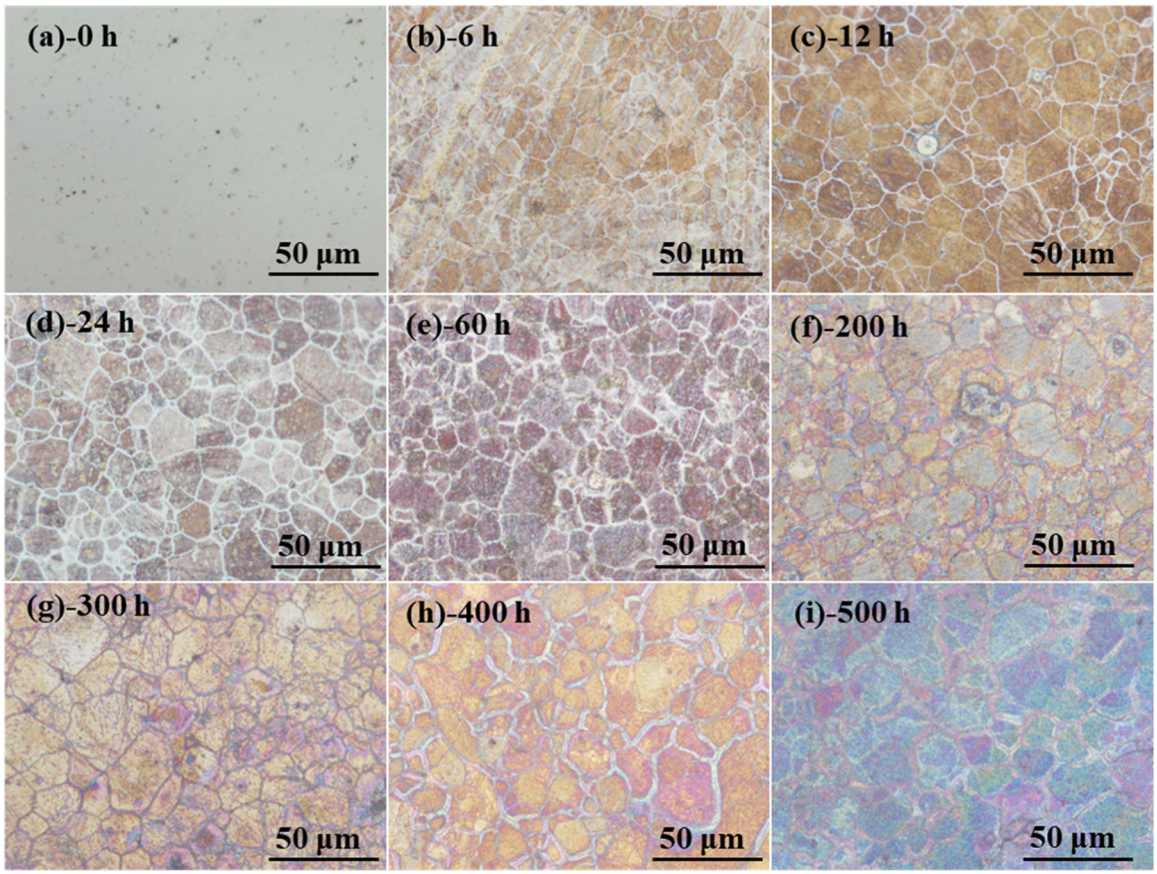

FIGURE 1 | Surface optical morphologies of the Mg–Y alloy after various oxidization times. [Color figure can be viewed at wileyonlinelibrary.com]

grain enhances. Moreover, the color of the sample surface has changed slightly from light yellow (Figure 1b,c) from yellowish gray (Figure 1d) to slightly purple (Figure 1e). Such color change is indicative of the composition or thickness evolutions of the oxidized scale, as the light reflectivity of metallic oxides is highly dependent on its thickness [35, 36] and compositions (probably MgO/Y_2O_3 ratio here).

When the sample had been oxidized for 200 h, the most noticeable changes can be observed around the aforementioned boundaries, as their color changed from white to bluish cast. Such change is possibly due to the formation of different oxidation products around those boundaries other than that had been formed in the shorter-time oxidized samples. The surface appearance of the oxidized scale remained almost unchanged even when the oxidation time increased to 400 h, except that the network boundaries became even thicker (Figure 1h). Nevertheless, substantial changes can be observed when the sample was oxidized to 500 h (Figure 1i). For instance, the sample surface exhibits a kind of blue-to-violet color, which coincides with the wavelength of the lightest reflectivity of yttria [37], suggesting that the Y_2O_3 content of the oxide scale might have been increased.

3.2 | Microstructural Characterization

Figure 2 exhibits the backscattered electron SEM images of the Mg–Y alloy isothermally oxidized at 350°C various times. As can be seen, the SEM images present quite consistent characteristics with that presented in Figure 1 in terms of the increasing grain boundary width as the oxidation time increases. As the contrast of the backscattered electron images is directly proportional to the probed atomic numbers, the bright areas shown in Figure 2 are believed to have higher Y contents. In this respect, it seems that surface chemical redistribution had occurred in the oxidation process, and Y atoms are more likely to segregate along the grain boundaries as the oxidation proceeds. It should be emphasized that Y segregation along the grain boundaries was also observed in the as-polished samples (Figure 2a). Such phenomenon is quantitatively analyzed using EDS, where the chemical compositions of the entire sample surface as well as some specific sites marked by yellow arrows were derived; the results are, respectively, shown by Figure 3 and summarized in Table 2. It is clearly shown in Figure 3 that the averaged Y content determined from the sample surface gradually increases with increasing oxidation times and is well above the nominal composition of the bulk alloy, suggesting Y segregation on the sample surface. Such segregation extent intensifies as the oxidation time increases. Apart from surface segregation, the Y atoms also tend to segregate along the initial grain boundaries. Specifically, the grain boundary (Site 1) of the 6 h' oxidized sample contains 1.41 at.% Y (Table 1), this value is well above that of the averaged Y content (0.86 at.%) of the sample surface (Figure 3). When the oxidation time increases further to 12 h and 48 h, the Y concentration at the grain boundaries increases accordingly

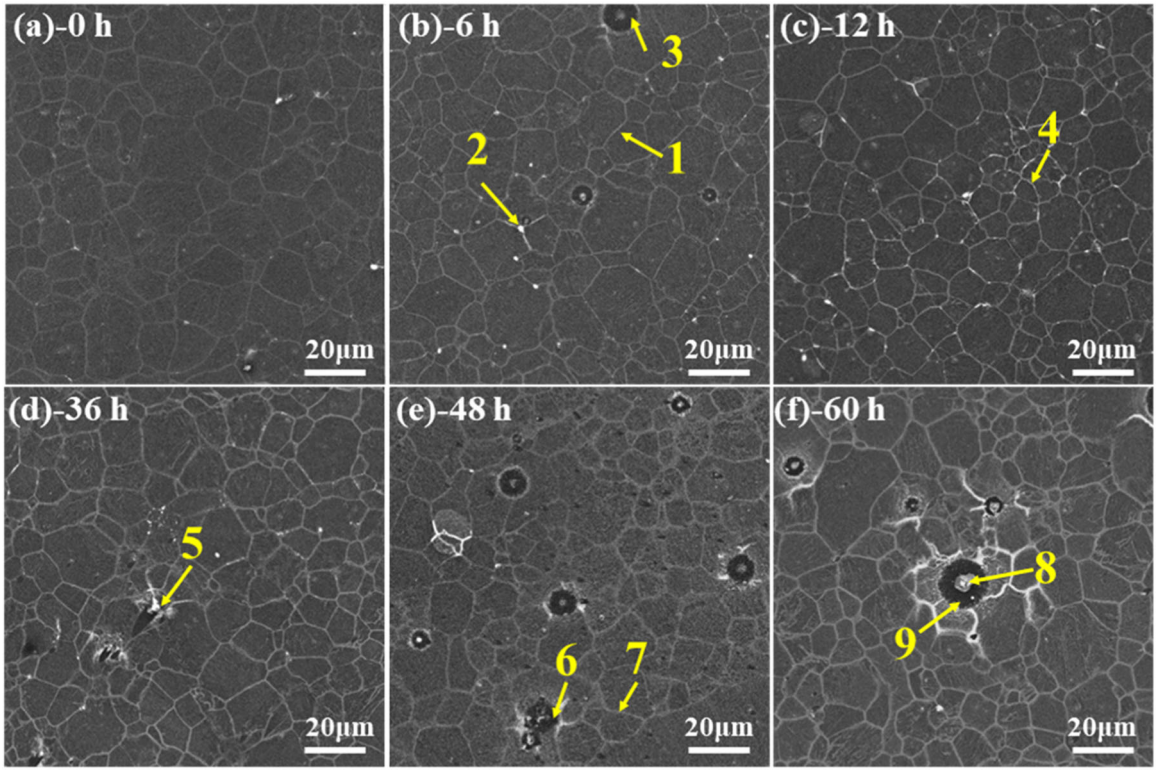

FIGURE 2 | Surface scanning electron microscopy (SEM) morphologies of the Mg–Y alloy after various oxidization times. [Color figure can be viewed at wileyonlinelibrary.com]

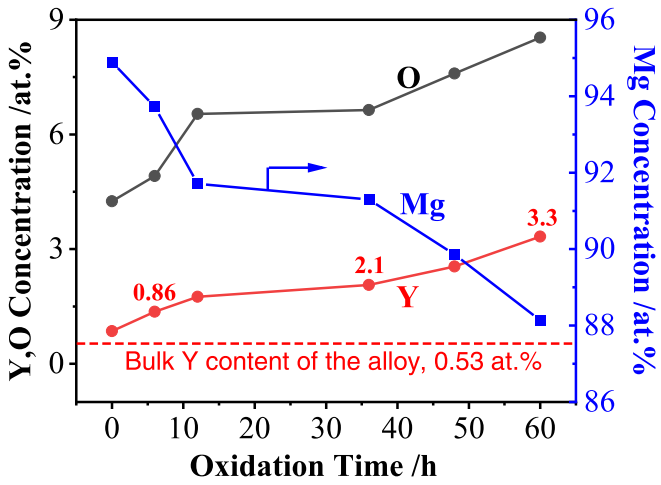

FIGURE 3 | Dependence of the averaged surface chemical evolution on the oxidation time of the Mg–Y alloy at 350°C. [Color figure can be viewed at wileyonlinelibrary.com]

to 1.91 at.% (Site 4) and 3.05 at.% (Site 7), respectively. The averaged O content on the sample surface and along these grain boundaries present the same trend as Y, while the Mg content evolution exhibits an opposite tendency (Figure 3). The decreased Mg content is only partially due to the increased content of (O + Y), but might also be due to the thickening of the oxide scales (so the EDS results are less affected by the Mg-substrate) as the oxidation time increases.

Moreover, the Mg–Y alloy also contains a lot of Y-rich secondary phase particles, as observed in Figure 1; such observation is even more straightforward in the SEM images, as proven by the white dots embedded in Figure 2a. Such secondary phase particles significantly affect the neighboring oxidation behavior, which in turn affects the composition of both these particles and that of the neighborhood regions. Site 2 shown in Figure 2b, is an example of the secondary particle that has been slightly affected by oxidization, and the Y content here is as high as 3 at.%. In this short-time oxidized sample, there are also particles that have been heavily affected by oxidation. For example, Site 3 in Figure 2b marks the region surrounding a secondary particle. It can be seen that the contrast of the particle has faded, suggesting the reduced Y content of the particle itself. Simultaneously, the particle was surrounded by an almost-perfect circle with a bright white edge and even darker regions between the edge and the particle. Such phenomenon is frequently observed in the Mg-Y alloy even when the oxidation time was increased to 48 h and 60 h, as shown in Figure 2. Lower Y content is expected in the dark regions (Y-depletion region), say Site 3, Site 6, and Site 9, surrounding the particles based on the imaging principles of the backscattered electrons. Actually, the Y content at Site 6 and 9 is only 0.75 at.% and 1.13 at.%, respectively. Such values are much lower than the averaged Y content, that is, 2.1 at.% and 3.3 at.%, on the sample surface oxidized for the same period of time.

More detailed surface chemical analysis of the sample oxidized at 350°C for 60 h is conducted by EPMA, and the results are depicted in Figure 4. The elemental segregations of Y and O along the grain boundaries are also verified according to the elemental mapping analysis, as shown by Figure 4c,d. Accordingly, the grain boundaries possess less Mg content than the grain interior (Figure 4b). Quantitative analysis of the chemical

TABLE 2 | The EDS analysis of the corresponding regions is shown in Figure 2.

	Regions as indicated in Figure 2								
Element (at.%)	**1**	**2**	**3**	**4**	**5**	**6**	**7**	**8**	**9**
O	4.17	6.71	4.62	6.74	6.24	2.93	9.06	29.44	3.25
Mg	94.36	90.22	94.43	91.35	91.52	96.32	87.89	59.52	95.62
Y	1.47	3.08	0.96	1.91	2.24	0.75	3.05	11.04	1.13

Abbreviation: EDS, energy dispersive X-ray spectrometer.

variations along the segments A and B perpendicularly crossing two different grain boundaries are respectively plotted in Figure 4e,f. It is clear that both the O and Y concentrations exhibit a Gaussian-type distribution, whereas the Mg content shows a valley-like distribution, with the extremums of all three plots observed exactly at the middle point of the grain boundaries. The chemical distribution profiles were fitted using the Gaussian formula, and the FWHMs (full-width at half maximum) of the fitted peaks, $0.50 \pm 0.05\,\mu m$, were taken as the width of the elemental segregated boundaries.

Based on Figure 4e, the Mg, O, and Y concentrations at the extremums (that can be roughly taken as the composition of the grain boundary) are extracted to be 86.8 at.%, 9.3 at.% and 3.9 at.%, respectively. Assuming that all the Y atoms are bonding with O to form stochiometric Y_2O_3 (the most common oxide of yttrium), then the O atoms taken by Y should be 5.8 at.%. Such a value is significantly lower than the detected O. The excessive O content (3.5 at.%) must have been bonding with Mg to form MgO. Therefore, the coexistence of Y_2O_3 and MgO is expected along the grain boundaries, and the molar fraction of Y_2O_3 in the oxide mixture is roughly 36.1%.

The Mg, O, and Y atomic concentrations at a distance away from the grain boundaries (as indicated by a dashed line in Figure 4e) were also extracted to roughly represent the chemical compositions in the grain interior, and the results are 92.9 at.%, 5.1 at.% and 1.7 at.%, respectively. Then it can be calculated (based on the same assumption that all the Y existed in the form of Y_2O_3 and all the O atoms were forming metallic oxides) that the molar fraction of Y_2O_3 in the oxide scale is 25.0%. Similar results can also be derived from the plot shown in Figure 4f). From the EPMA analysis, it can be concluded that (i) the oxide scale formed on the Mg-Y alloy surface comprises Y_2O_3 and MgO, and (ii) the original grain boundaries seem to facilitate the formation of Y_2O_3.

The surface morphologies of the alloy after 60 h' oxidation were also characterized using AFM, and the results are shown in Figure 5a. The height profiles along segments perpendicularly crossing the grain boundaries (as numbered in Figure 5a) were also extracted, and the results are plotted in Figure 5b). It should be mentioned that each curve has been shifted to make the middle of each grain boundary the zero point of the x-axis. The inset in Figure 5b shows the height profile along Segment 1; it is clear that the grain boundary is appreciably higher than that of the adjacent grain interiors, and the resulting height profile exhibits good symmetry and follows the Gaussian distribution (as indicated by the solid red line in the inset). All of the height profiles present the same distribution; therefore, they are not discriminated in Figure 5b. It is now clear that the higher grain boundary, other than the grain interior, seems to have a regular pattern. By fitting these curves against the Gaussian formula and averaging the full width at half maximum (FWHM) of each peak, the averaged width of the grain boundaries is derived approximately to be $0.63 \pm 0.1\,\mu m$ (slightly higher than that derived from the elemental distribution shown in Figure 4e,f probably due to the difference in the spatial resolution of EPMA and AFM). The height of the grain boundaries above the neighboring grains, calculated as the average of the peak heights, is 24.7 ± 5.2 nm. Considering that the samples had been carefully polished before oxidation, the sample surface should not have shown such lateral height differences had the grain interiors and boundaries experienced the same oxidation rate. Therefore, the lateral height difference might indicate different oxidation rates at the grain boundaries and grain interiors. The higher height of the grain boundaries than the grain interiors can also be rationalized from the regional chemical analysis. The higher grain boundaries might suggest a higher content of Y_2O_3 at the grain boundaries other than the grain interiors. Since the conversion of Y to Y_2O_3 leads to an increased volume, while the formation of MgO is associated with a decreased volume, the aggregation of more Y_2O_3 at the boundary certainly results in an increased regional height.

3.3 | Phase Composition Analysis by XRD

XRD analysis was implemented to determine the phase composition, as well as its dependence on oxidation time, of the Mg–Y alloy isothermally oxidized at 350°C, and the results are plotted in Figure 6. Sharp and apparent peaks at $2\theta = 32.1°$, 34.4°, 36.6°, 47.8°, and 57.3° are observed in all the diffraction patterns, which are, respectively, associated with the (100), (002), (101), (102) and (110) crystallographic planes of the α-Mg phase (PDF #04-0770) following the simple search/match method. This phase is directly related to the Mg–Y substrate. Moreover, it is clear that the intensities of the α-Mg peaks gradually reduce, the α-Mg (002) peak in particular, because fewer X-rays can reach the substrate as the thickness of the oxide scale increases with increasing oxidation time.

It is not surprise that the secondary phase $Mg_{24}Y_5$ observed in Figure 1 and Figure 2 is not detectable in the as-polished samples because of its too low volume fraction in the as-extruded alloy. Nevertheless, the oxidation temperature utilized in the present study will facilitate the precipitation of the secondary phases, as had been reported by Zhang et al. [38]. Therefore, a peak at around $2\theta = 29.8°$ is observed as the oxidation time increases beyond 12 h, which is believed to arise from the (321) crystallographic planes of the secondary phase $Mg_{24}Y_5$ (PDF #16-0854). It should be mentioned that the

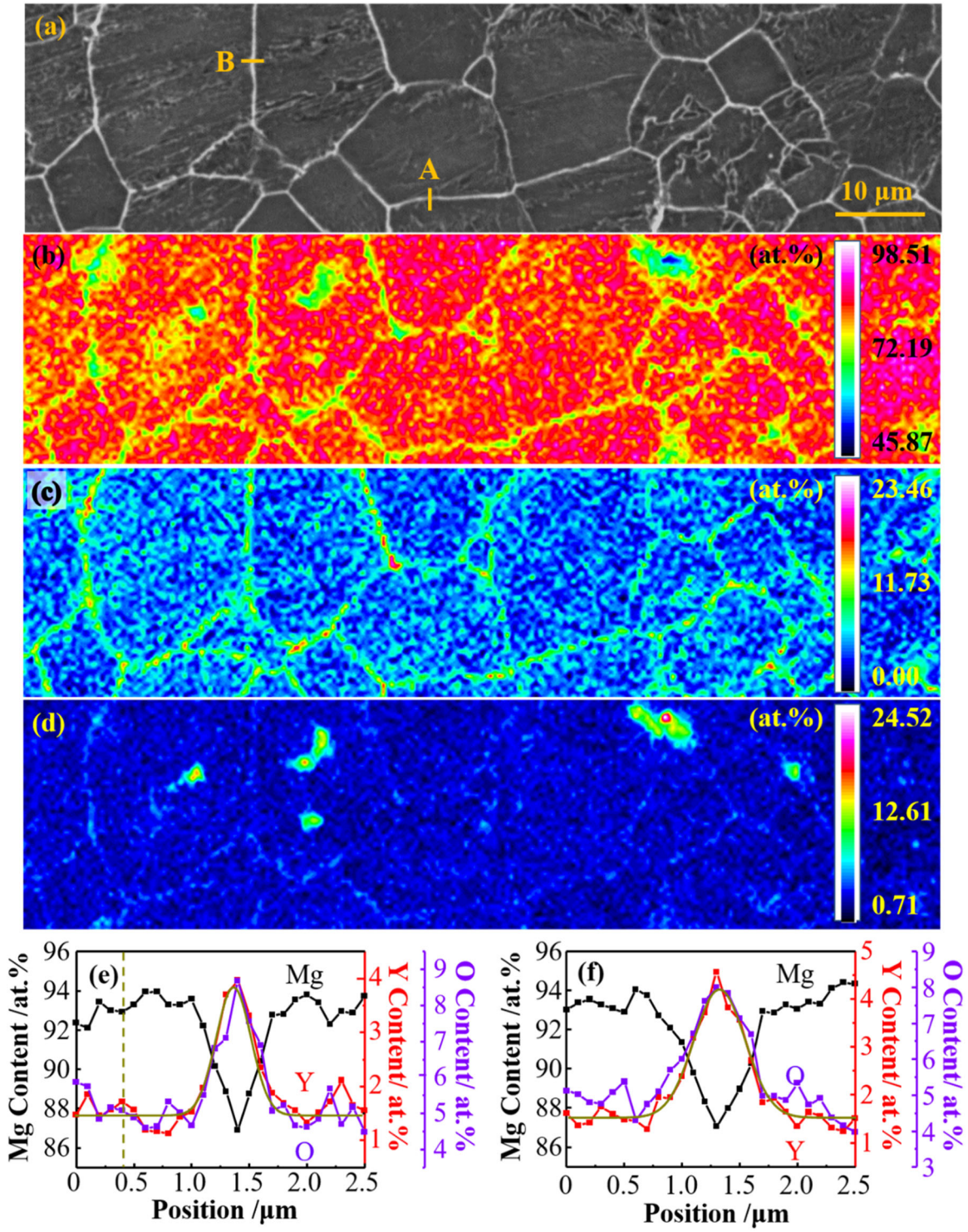

FIGURE 4 | (a) Surface morphology of the Mg–2Y alloy oxidized at 350°C for 60 h, the corresponding surface chemical distribution of (b) Mg, (c) Y and (d) O and the chemical distributions crossing, (e) the grain boundary A, and (f) grain boundary B marked in (a). [Color figure can be viewed at wileyonlinelibrary.com]

volume fraction of the $Mg_{24}Y_5$ phase cannot increase sustainably because of the low Y content of the studied alloy. Also, due to the continuous thickening of the oxide scale, the penetration of the incident X-rays toward the substrate is reduced. These two factors, that is, a limited amount of $Mg_{24}Y_5$ and thickening of the oxide scale, lead to the diminishing of the $Mg_{24}Y_5$ (321) peak as the oxidation time increases beyond 60 h, and this peak cannot be detected when the sample was oxidized for longer than 500 h.

Apart from the peaks associated with the α-Mg and $Mg_{24}Y_5$, additional peaks can also be identified in the oxidized sample. To be specific, peaks at $2\theta = 20.4°$, 29.0° and 33.8° were detected when the sample was oxidized for > 12 h, and another weak

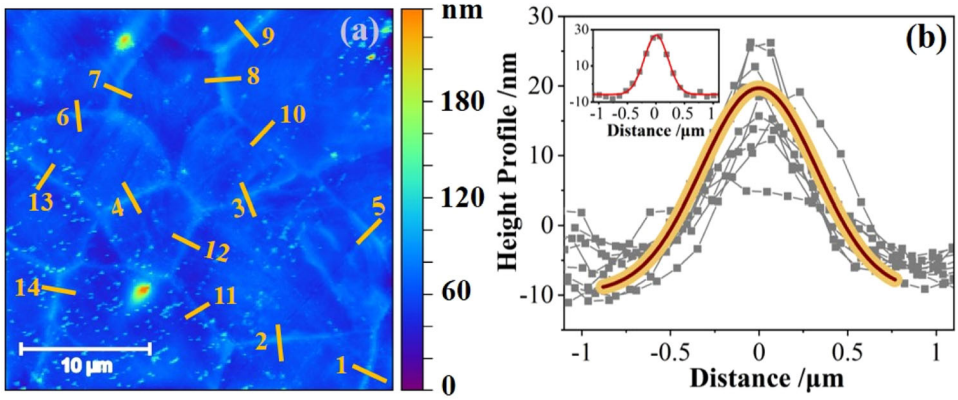

FIGURE 5 | (a) Atomic force microscope (AFM) analysis of the sample oxidized at 350°C for 60 h and (b) the height profiles of the segments labeled in (a). [Color figure can be viewed at wileyonlinelibrary.com]

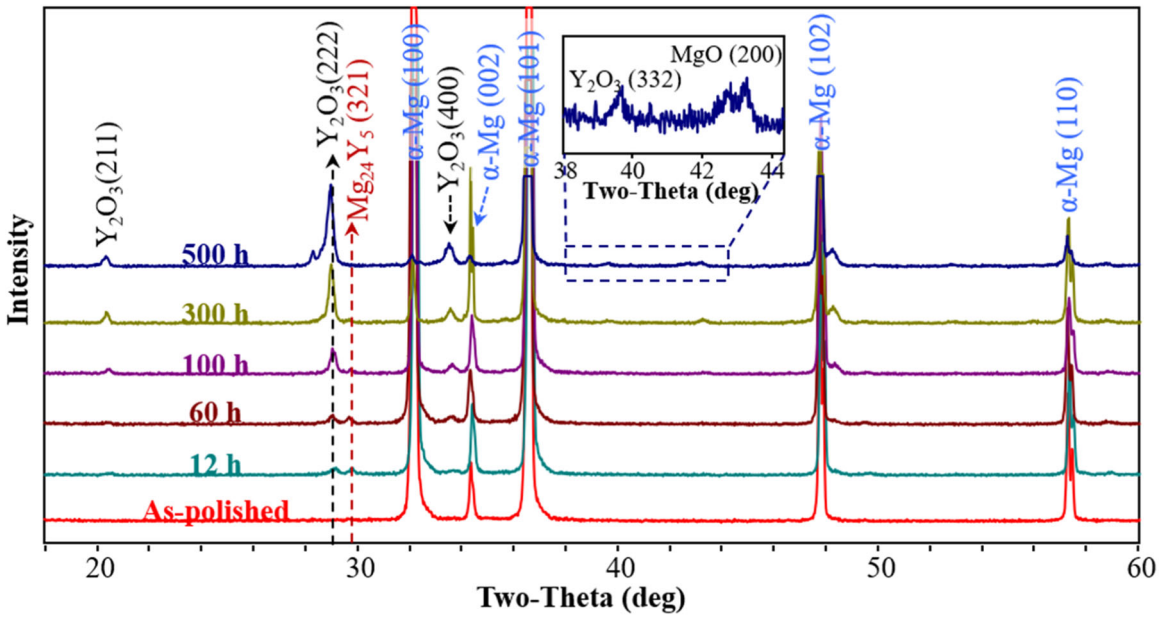

FIGURE 6 | X-ray diffraction (XRD) patterns of the Mg–2Y alloy oxidized at 350°C for various time. [Color figure can be viewed at wileyonlinelibrary.com]

peak at $2\theta = 39.8°$ appeared as the oxidation time is > 300 h. These peaks perfectly match the standard powder diffraction pattern of the Y_2O_3 (PDF #25-1200). Therefore, the Y_2O_3 phase was formed in the oxidization process. Moreover, all the Y_2O_3 peaks present well-defined sharp Bragg peaks, suggesting that the Y_2O_3 phase is well crystallized.

Moreover, when the alloy was oxidized at 350°C for longer than 100 h, an additional peak at $2\theta = 42.9^{o}$ appears even though its strength is pretty weak (the inset in Figure 6). By considering the chemical compositions of the oxidized sample and searching for the PDF database, it is straightforward that this peak can be attributed to the MgO (200) (PDF # 43-1022) diffraction. The coexistence of the Y_2O_3 and MgO, proven by the XRD results, is also consistent with our speculations based on the EPMA and EDS results. It should also be noted that the intensities of the peaks associated with Y_2O_3 and MgO had been gradually strengthening because of the progressive thickening of the oxidized scales.

3.4 | Surface Chemical Analysis by XPS

The XPS survey spectra of the samples oxidized at 350°C at various times are exhibited in Figure 7. In the as-polished sample without oxidation, signature peaks are observed around 530 eV, 347 eV, 285 eV, 89 eV, and 52 eV, associated with O 1*s*, Ca 2*p*, C 1*s*, Mg 2*s*, and Mg 2*p*. The Ca content in the sample is inevitable because the feeding raw material Mg in the casting procedure (to prepare the current Mg-Y alloy) was prepared by reducing $MgCa(CO_3)_2$ through the Pidgeon process. However, it is hard to detect any yttrium signals in the as-polished sample. When the sample was oxidized at 350°C even for a short time, say 6 h, the Y 3*d* peaks appeared at around 158 eV, as an indicative of Y segregation toward the sample surface during oxidation. Other than the appearance of the Y 3*d* peak, the presence of the signature peaks excited from the rest species persisted. When the oxidation time was further prolonged to 60 h, the characteristics of the XPS spectra remained almost unchanged, suggesting that the oxidation time did not

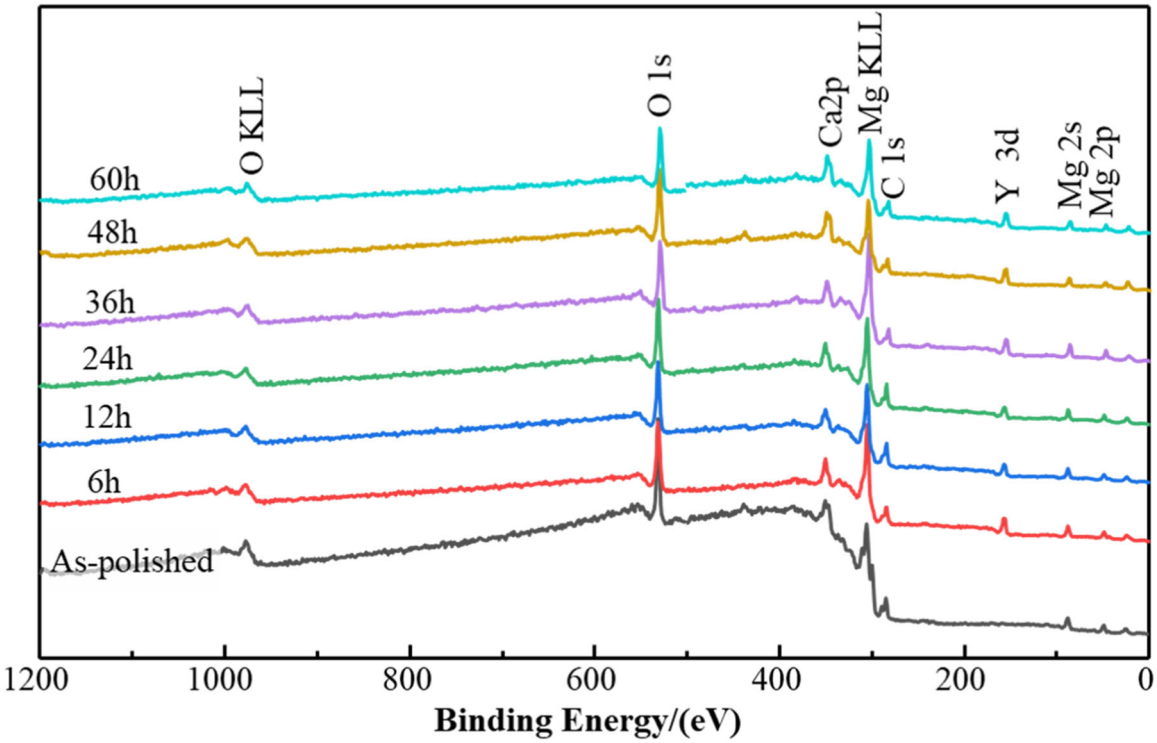

FIGURE 7 | X-ray photoelectron spectroscopy (XPS) survey spectra of the Mg–2Y alloy oxidized at 350°C for various time. [Color figure can be viewed at wileyonlinelibrary.com]

significantly alter the chemical valent states on the sample surfaces (as the XPS penetration depth is only limited to around 10 nm).

The high-resolution XPS spectra of the C 1*s*, O 1*s*, Mg 2*p*, and Y 3*d* transitions were also collected after various oxidation times, which, together with their respective deconvolution analysis, are exhibited in Figure 8. As seen from the first column of Figure 8, the C 1*s* spectra did not present any significant changes as the oxidation time increased. The deconvolution of the C 1*s* spectra yielded three sub-peaks at BE = 284.8 eV, 289.7 eV, and 285.7 eV, associated with the adventitious carbon, carbonates, and C–O–C components, respectively. The Mg 2*p* spectra obtained from the freshly-polished Mg–Y overlap with the Mn 3*p* (BE = 48.4 eV) (Figure 8b). Mn raised from the impurities of the studied Mg–Y alloy (as shown in Table 1). The Mg 2*p* peaks dominated around the binding energy of 50 eV can be resolved into two subpeaks, say $2p_{3/2}$ and $2p_{1/2}$ peaks, at a separate binding energy of 0.28 eV and peak intensity ratio of 2:1 due to the orbital splitting. The binding energy of the Mg $2p_{3/2}$ peak is determined to be 49.9 eV, suggesting that the Mg atoms on the freshly polished sample existed in their metallic state (Mg°). When the samples were oxidized at 350°C, the Mn 3*p* spectra could not be detected anymore due to the formation of an oxide scale on the sample surface. The deconvolution analysis of the Mg 2*p* peaks suggests the coexistence of metallic Mg (Mg°. BE = 49.5 eV) and MgO (BE = 50.3 eV) on all the oxidized sample surface regardless of the oxidation time (The $2p_{3/2}$ and $2p_{1/2}$ splitting doublets are not included in Figure 8b due to their narrow BE gap). The as-polished sample surface yielded a single O 1*s* peak that can be deconvoluted to three O 1*s* transitions, i.e., metallic oxides (BE = 529.6 eV), carbonates (BE = 531.6 eV) and OH^- (BE = 532.5 eV) [39]. The presence of the OH^- component might be attributed to the inevitable moisture absorption on the sample surface. When the sample was oxidized, the three transitions of O 1*s* can all be resolved from the O 1*s*. Nevertheless, the ratio of the three sub-peaks has to be adjusted to accommodate the ever-changing of the FWHMs as the oxidizing time increases.

The intensity of the spectrum acquired from the as-polished sample surface in the BE range of 162–154 eV was very weak, yielding a high noise/signal ratio. However, the splitting doublets associated with the Y $3d_{5/2}$ and Y $3d_{3/2}$ orbitals with a BE gap of 2.1 eV are still distinguishable. The Y $3d_{5/2}$ peak can be observed at BE = 158.1 eV, suggesting the presence of $Y_2(CO_3)_3$ [40]. After polishing, a marginal amount (0.3 at.% as quantified by XPS analysis) of Y atoms was presented on the sample surface, which then reacted readily with the surrounding air to form Y_2O_3, the only stable oxides of yttrium. Subsequent adsorption of CO_2 in the atmosphere on the Y_2O_3 leads to the formation of yttrium carbonates [41]. The identification of the $Y_2(CO_3)_3$ was also cross-verified by the presence of a carbonate component (BE = 531.6 eV) from the O 1*s* deconvolution analysis. When the sample was oxidized for 6 h, the concentration of Y at the sample surface increased to tenfold that of the bulk alloy, leading to a well-defined Y 3 *d* spectrum that can be resolved into two pairs of splitting-doublets (each pair is marked using the same color in Figure 8d). The two splitting doublets are ascribed to Y_2O_3 (Y $3d_{5/2}$ BE = 157.0 eV) and $Y_2(CO_3)_3$ (Y $3d_{5/2}$ BE = 158.3 eV), respectively. As the samples are oxidized for a longer time (< 60 h), the coexistence of the two Y-containing components persists, and the Y content at the outmost surface remains at a high level of 3.3–5.1 at.% that is well above the bulk composition of the studied alloy, suggesting a Y enrichment on the sample surface during the oxidation process.

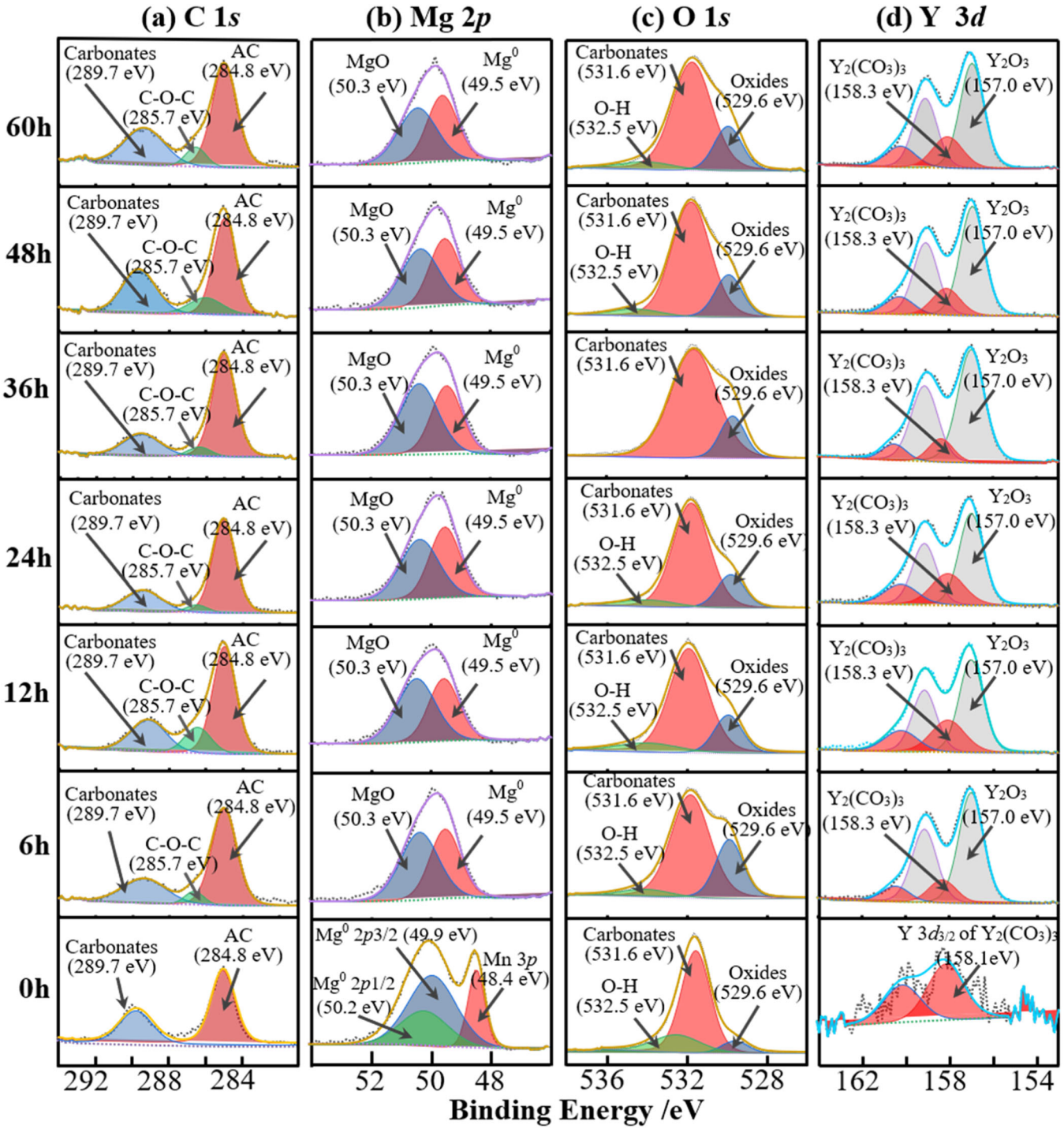

FIGURE 8 | High-resolution X-ray photoelectron spectroscopy (XPS) spectra excited from orbitals of (a) C 1*s*, (b) Mg 2*p*, (c) O 1*s,* and (d) Y 3*d* from the Mg–2Y alloy oxidized at 350°C for various times. [Color figure can be viewed at wileyonlinelibrary.com]

To understand the oxidation kinetics of the Mg–Y alloy, the sample oxidized at 350°C for 60 h was sputter etched using Ar^+ ions, and the survey,and high-resolution XPS spectra were, respectively, collected to disclose the chemical depth distribution (Figure 9). It should be mentioned that the intensities of the spectra had been normalized to assure the reliability of the direct comparison among the spectra. It is clear that Mg, O, C, and Y are detected from the surface of the oxidized, as consistent with the EPMA results. However, the relative content of these elements varies significantly as the sputtering time increases. For example, an intense C 1*s* peak was observed from the as-oxidized sample without any sputter etching, and the strength of the C 1*s* peak is comparable to that of Mg, O, and C. The presence of C 1*s* signal may be ascribed to carbon contamination (adventitious carbon) or adsorption of carbon dioxide [42] while exposure to air. However, it seems that such carbon contamination is only confined to the top-most of the sample surface, as the C 1*s* signal can hardly be identified in the survey spectrum after only 3 min' etching by the Ar^+ ions (as shown by the inset in Figure 9). After the removal of the carbon layer, all of the peaks associated with the O 1*s*, Y 3*d,* and Mg 2*s* became intensified. To make such a tendency more

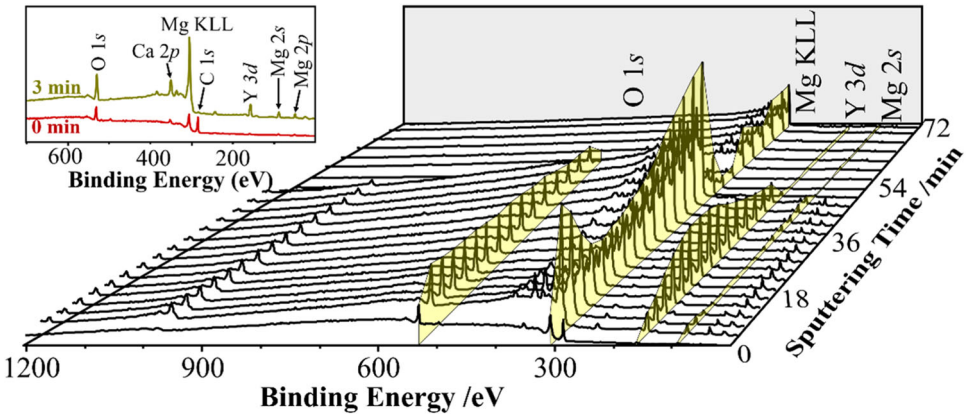

FIGURE 9 | The X-ray photoelectron spectroscopy (XPS) survey spectra from the Mg–Y alloy oxidized at 350°C for 60 h after sputter etching various times. [Color figure can be viewed at wileyonlinelibrary.com]

visibly apparent, the highest points of the respective peaks are connected and marked using yellow shades in Figure 9.

The peak around the binding energy of 530 eV associated with the O 1*s* was significantly increased after 3 min' sputter-etching. Such O 1*s* signal must have raised from the oxide scale, the intensity of which is gradually diminishing with the increasing etching time. It suggests a reducing O content from the surface towards the bulk of the oxide scale. The evolution of the peak intensity associated with Y 3*d* orbits is much more complicated than that of the O 1*s* peak. To be specific, the intensities of the Y 3*d* peaks exhibited an inverted "U-shaped" pattern along with the increasing etching time. Its peak strength gradually increases as the etching time increases up to 21 min; afterward, the Y 3*d* peak gradually weakens. The evolutions of the Mg 2*s*, as well as the associated Mg *KLL* peaks, are contrary to that of the Y 3*d* peaks and exhibit a normal 'U-shaped' parabolic pattern in the studied etching time range (3–72) minutes. To be specific, after the removal of the top-most carbon coverage (after 3 min' etching), both Mg peaks intensified. Then, with the increasing etching time, the intensities of the two Mg peaks decreased gradually and reached a minimum after being etched for 25 min. Then when the spectra were sampled from the deeper region within the oxide scale (etched for > 25 min), the Mg peaks gradually intensified. The overall evolutions of O 1*s*, Mg 2*p* (as well as Mg *KLL*), and Y 3*d* with the oxidize depth suggest an inhomogeneous chemical distribution along the oxide thickness that might provide insights into how the oxide scale was formed.

To verify the chemical evolutions with etching time, the high-resolution spectra of the C 1*s*, Mg 1*s*, O 1*s*, and Y 3*d* were also acquired within their respective binding energy ranges, as shown in Figure 10. It should be mentioned that each curve in Figure 10 was rescaled to different Y-axis ranges. We did not attempt to deconvolute the spectra shown in Figure 10 because of the lack of reliable BE calibration. It is impractical to align the BE scales using the C 1*s* referencing because of the absence of the adventitious carbon on the sample surface after 9 min' etching. Moreover, the oxide scale did not exhibit any Fermi level (FL) cut off, which makes it difficult to derive the '0' point on the BE scale [43]. Hence, the high-resolution spectra are shown as recorded. Fortunately, this inability to make BE calibration did not prevent us from investigating the relative spectral changes with etching time.

In the as-oxidized (etching time = 0 min) sample surface, the C 1*s* spectrum displayed a well-defined single peak at around 285 eV. When the sample was etched for 9 min, a weak C 1*s* peak could still be acquired, but its position had been shifted toward the lower BE direction to around 283 eV. Further increasing the etching time, the C 1*s* signal could hardly be detected. The Mg 1*s* spectra changed dramatically with increasing etching time, as shown in Figure 10b. To be specific, the Mg 1*s* spectra comprised only a signal peak with apparent symmetry when the etching time was < 21 min. When the sample was sputter etched for 21 min, the symmetry of the Mg 1*s* peak had been compromised with a dragging tail in the lower binding energy side. The Mg 1*s* spectra did not present any dramatic change when the etching time was 21–36 min (not shown here). Nevertheless, when the etching time was increased to 39 min, the Mg 1*s* shifted toward the higher BE direction, and a lower shoulder at the lower BE side was also observed. Such characteristics roughly persisted even when the sample was etched for 72 min.

Figure 10c indicated that when the etching time increased from 0 to 9 min the BE of the O 1*s* shifted from 532 eV to 531 eV; then, when the etching time was further increased to > 21 min, the BE of the O 1*s* shifted back to 532 eV. In addition, the O 1s peak only comprised a single symmetric peak when the sample was etched for up to 9 min. However, when the etching time increased to ≥ 21 min, an additional peak at 534 eV appeared apart from the main peak at 532 eV.

Normally, the 3*d* orbital-splitting yields a pair of doublets in the XPS spectra; however, the Y 3*d* spectra acquired in the etching time of < 9 min did not present any apparent doublets, possibly due to the coexistence of several different Y-containing compounds. However, when the sample was etched for 12–45 min (only the spectra acquired after 21 and 39 min' etching are shown in Figure 10d), the splitting doublets became apparent, with the $3d_{5/2}$ at BE = 159 eV, and a BE gap of around 2.05 eV. When the etching time was increased to 45–54 min (the spectra associated with 51 min' etching were presented as an example), the doublets of the Y 3*d* spectra could not be distinguished, yielding a single peak similar to that of the un-etched sample. The distinguishable

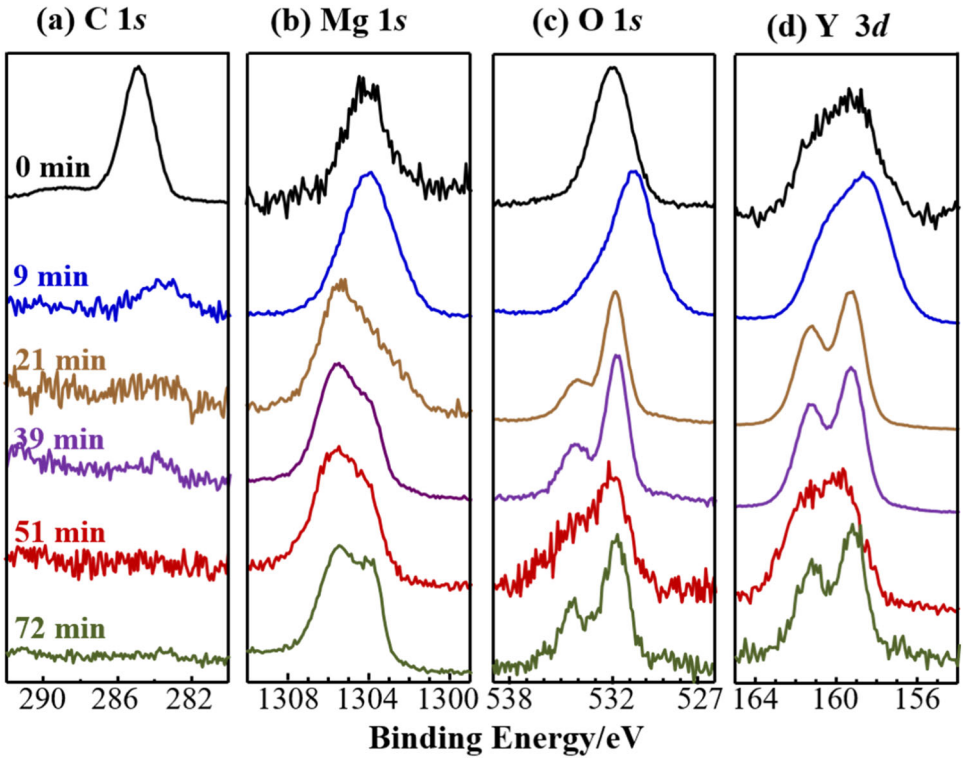

FIGURE 10 | The (a) C 1*s*, (b) Mg 1*s*, (c) O 1*s*, and (d) Y 3*d* X-ray photoelectron spectroscopy (XPS) high-resolution spectra acquired from the Mg–Y alloy oxidized at 350°C for 60 h after sputter etching for various time. [Color figure can be viewed at wileyonlinelibrary.com]

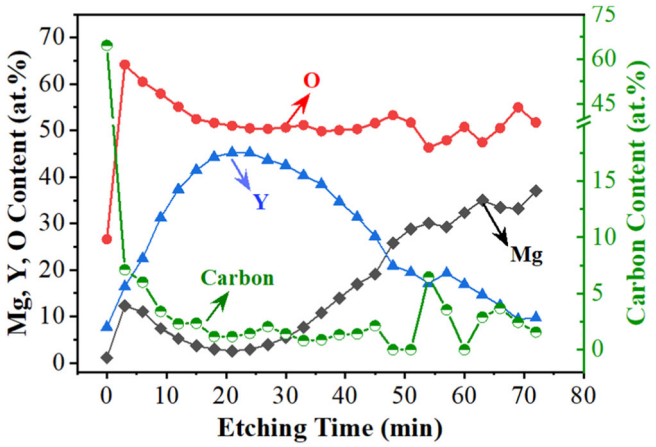

FIGURE 11 | The evolution of the atomic contents of Y, Mg, O, and C with the etching time. [Color figure can be viewed at wileyonlinelibrary.com]

doublets could be observed again when the etching time was 54–72 min.

The spectral changes shown in Figure 10 suggested that the bounding situation of the various chemicals varied through the thickness of the oxide scale. Even though it is unreliable to conduct deconvolution analysis as explained, the spectral changes can still be indirectly rationalized by quantitatively analyzing the chemical concentrations based on the high-resolution XPS spectra shown in Figure 10. In this regard, the evolutions of the Mg, O, C, and Y concentrations along with the etching time was quantified and the results are displayed in Figure 11. As can be seen, the carbon content on the sample surface drops significantly from around 64.58 at.% to a level of around 2–3 at.%, when the etching time increased from 3 min to 50 min. Therefore, a thin layer of carbon contamination covering the sample surface was formed in the time interval between isothermal oxidation and XPS characterization. The low C content in the bulk of the oxides (etched for 10–15 min) might come from the CO_2 adsorption during the XPS acquisition [42]. As the sample was sputter etched for 54 min, however, the C content increased abruptly to 6.5 at.%, and further prolonging the etching time, the carbon content reduced significantly to a low level. The localized spiking carbon content in the middle might have arisen from carbon contamination (AC) from the atmosphere before the as-polished sample was subjected to isothermal oxidation. In this regard, it can be speculated that the depth reached after 54 min′ etching is adjacent to the boundary between the naturally formed sample surface and the artificially formed oxides.

The pattern of the variation in Mg content was contrary to that of Y by exhibiting a "U-type" characteristics. When the sample was etched from 3 to 21 min, the corresponding Mg content dropped from 12.28 at.% to 2.60 at.%. Further increasing the etching time to 72 min, the Mg contents increased monotonically to 36.98 at.%. The O content reduced gradually with the increasing etching time. As has been verified in Figure 9, the Y content variation presented an inverted "U-type" pattern along with the etching time, that is, Y content increased from 16.43 at.% to 45.23 at.% when the etching time increased from 3 to 21 min, afterward the Y content dropped gradually to 9.72 at.% after 72 min′ etching. It should be mentioned that after

72 min' etching, the Y content was still almost 20 times that of the bulk composition of the studied alloy. Such high Y content suggests an oxidation-affected Y-segregation at the interface between the artificially formed oxides and the bulk metallic substrate.

Quantitative analysis of the chemical composition at the position of the 72 min etched sample revealed the C, Y, O, and Mg concentrations of 1.58 at.%, 9.72 at.%, 51.72 at.%, and 36.98 at.%, respectively. Adapting the assumption that C originated from the C contamination during XPS characterization, it is plausible that Y and Mg atoms had combined with O to form respective stoichiometric oxides Y_2O_3 and MgO based on the fact that the atomic concentration of O equals exactly the sum of $1.5 \times Y + Mg$. Therefore, the oxide scale had not been completely removed even after 72 min etching. Similar stochiometric oxides have also been verified on the topmost surface of the samples based on chemical analysis and deconvolution analysis of the as-oxidized samples.

On the other hand, a higher $1.5 \times Y + Mg$ value than the O content suggested the formation of an oxygen-deficient Y_2O_3 and MgO scale. Based on this criterion, it can be found that the bulk of the studied oxide scale (the etching time between 9 and 63 min) was apparently O-deficient, and the deficiency of O varies along with the scale thickness.

3.5 | Oxide Scale Characterization by TEM

The cross-sectional image of the sample oxidized at 350°C for 60 h was thinned using FIB and then subjected to TEM observation, as shown in Figure 12. The bright filed image shown in Figure 12a as well as the chemical mapping images all exhibited a continuous layer of oxide scale with high compactness. The chemical distribution of the cross-sectional TEM images is presented in Figure 12b. It is clear that a thin Mg-enrichment layer was covering the whole sample surface. The Y atoms were mainly localized in the region between the superficial Mg layer and the Mg–Y substrate. And the O atoms could be observed through the entire oxide.

From the bright field image shown in Figure 12a, it seems that thicker oxide scales normally took place around regions of different contrasts. One of the regions was designated as (D), and the chemical analysis of this region revealed a concentration of Mg (73.9 at.%), Y (4.8 at.%), and O (21.3 at.%), suggesting that it might be the secondary phase $Mg_{24}Y_5$. However, the outward transportation of Y during the isothermal oxidation had led to a depletion of Y (respective to $Mg_{24}Y_5$) in this region (and also led to a Y-segregation on the sample surface). The Y-depletion observed might also be caused by the local evaporation because of the regional temperature rise (the oxidation process is generally exothermic). Therefore, severer localized oxidation had taken place around the secondary phases of the bulk alloy, as had been speculated from the optical (Figure 1) and SEM morphologies (Figure 2).

The selected area electron diffraction (SAED) analysis was conducted in regions marked as (A), (B), and (C), and the results are displayed in Figure 12c–e, respectively. It is clear that region (A), the interface between the oxide scale and the substrate, mainly contained MgO and α-Mg. The radius of the two circles is approximately equal to 1.4, which is consistent with

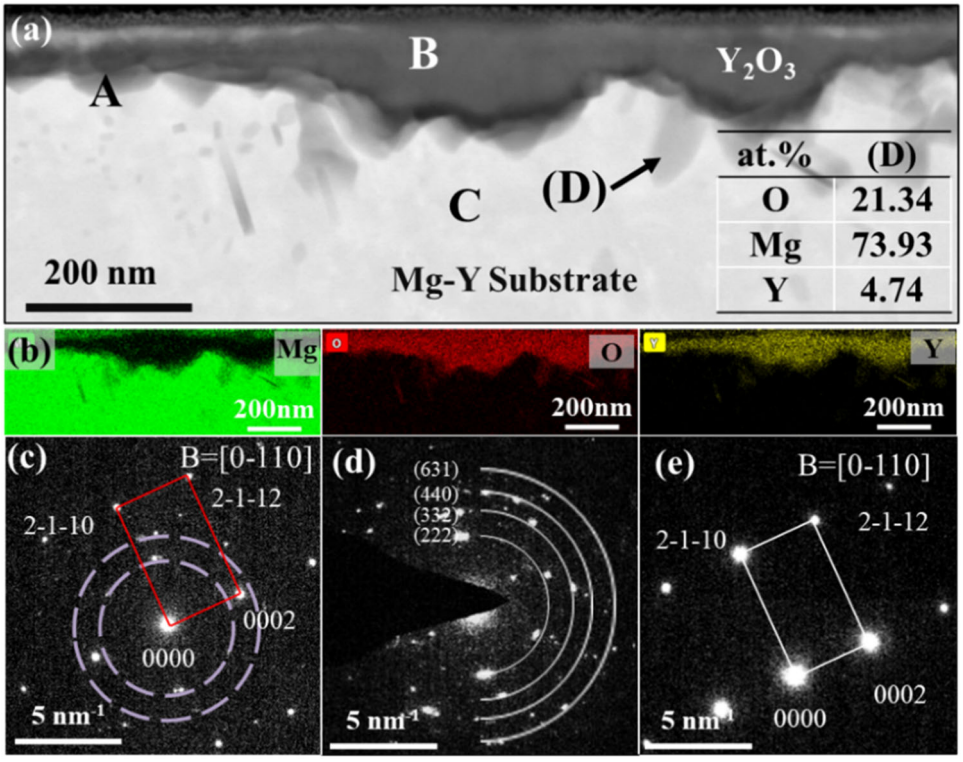

FIGURE 12 | (a) Transmission electron microscopy (TEM) cross-sectional bright filed image of Mg–2Y alloy oxidized at 350°C for 60 h; (b) the chemical mapping analysis along the thickness of the oxidized scale; (c), (d), and (e) the selected area electron diffraction of the regions A, B, and C, respectively, as marked in (a). [Color figure can be viewed at wileyonlinelibrary.com]

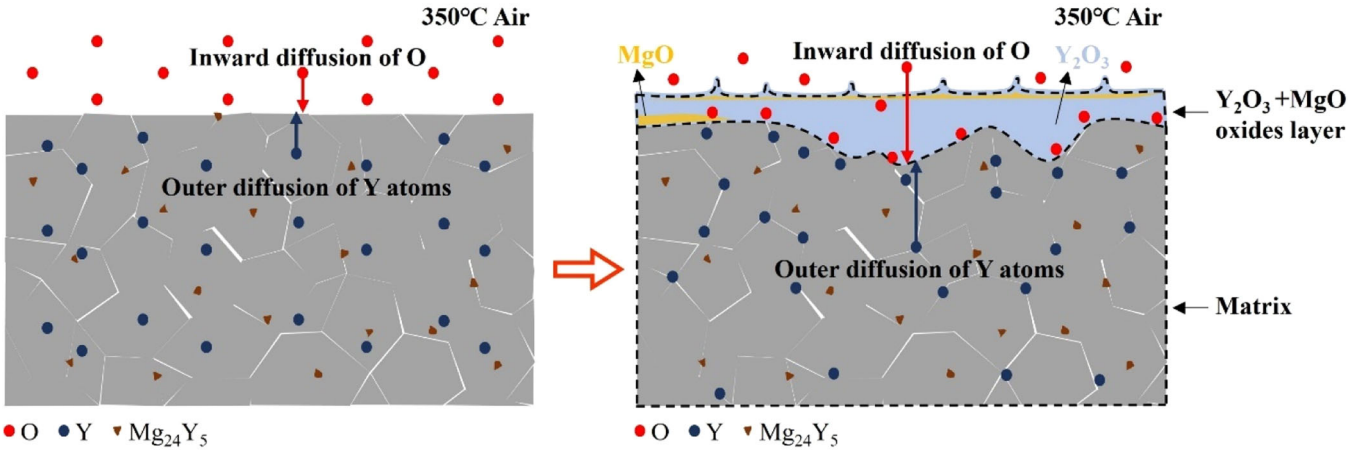

FIGURE 13 | Schematic illustration of the oxide scale structure formed on the Mg–Y alloy at 350°C in air. [Color figure can be viewed at wileyonlinelibrary.com]

the MgO powder diffraction. The crystallite size of MgO is small, and there is no preferred orientation, so no obvious diffraction spots are formed, while in regions (B), a dominant Y_2O_3 with good crystallization was identified. Unsurprisingly, only α-Mg can be observed in Region (C). The TEM diffraction results present good consistency with that of the XRD analysis.

3.6 | Discussion on the Oxidation Mechanism of the Mg–Y Alloy

Based on the composition of the oxide scale and the distribution of elements, a schematic diagram of the oxidation process for the Mg–Y alloy is proposed (Figure 13). The isothermal oxidation leads to the surface segregation of Y and also the growing of an oxygen-deficient Y_2O_3 + MgO layer on the sample surface of the Mg–Y alloy. The Y_2O_3 is the majority component in the oxide mixture. It has been widely accepted that Y has much better oxygen affinity than Mg; therefore, a diffusion of Y atoms from the bulk of the sample toward its surface, where the Y atoms may react with the surrounding O_2 to form a preliminary oxide scale. Nevertheless, the further thickening of the oxide scale does not take place by aggregation of the oxide on top of the preliminary oxides but instead by the gradual formation of oxides at the oxide scale/substrate interface, as supported by the following facts:

i. the Y_2O_3 oxide is actually a n-type semiconductor, showing anionic conduction. Then the transportation of the Y cations from the substrate to the oxide surface was very hard, if not impossible [44]. On the contrary, the O anions transport easily from the sample surface (where an excessive amount of O exists in the atmosphere) through the existing Y_2O_3 scale toward the interface, where they meet with the Y cations and combine to form the Y_2O_3;

ii. the irregular interface observed in the TEM bright images (Figure 12) is also supportive of the inwards-thickening of the oxide scale;

iii. the oxygen content through the oxide scale reduced gradually from the surface to the bulk of the oxides was another indicative of the inwards-thickening of the oxide scale. Since there is a sufficiently high amount of O at the sample surface during oxidation, any Y cations that appeared on the sample surface would have a good chance to react with O to form Y_2O_3. If the oxide scale thickening was realized by the outward Y transportation, then a constant O content through the oxide thickness should have been identified;

iv. the excessive amount of O around the sample surface and the high O affinity of Y may lead to stochiometric (rather than O-deficient) oxides that had the scale thickening governed by the outward Y transportation.

It should be mentioned that the anion transportation was also affected by the characteristics of the substrates, that is, the transportation along the initial grain boundaries was much faster than within the lattice because of the so-called short-circuit diffusion [45]; therefore, the grain boundaries presented localized increased surface out of the flat oxide scale surface.

4 | Conclusions

In summary, a Mg–Y binary alloy was isothermally oxidized at 350°C in air, and the surface changes during the oxidation process was systematically studied in the present study. Our results have demonstrated appreciably higher Y content, on the sample surface as well as along the initial grain boundaries, than that of the bulk alloy, suggesting a Y-segregation when the Mg–Y alloy was subjected to isothermal oxidation; Inhomogeneous oxidation took place because of the chemical/microstructure inhomogeneity of the original bulk alloy, that is, the initial grain boundaries experienced a higher oxidation rate other than the grain interiors, and the most severe localized oxidation was observed around the initial secondary phase particles; A compact layer of O-deficient Y_2O_3 + MgO scale was verified to form on the sample surface, with the yttrium oxide dominated the oxide mixture. It was discussed that oxide scale thickening involves the diffusion of Y atoms from the substrate to the oxide/substrate interface, the transportation of oxygen anions through the oxide scale toward

the interface, and finally, the O and Y reacted at the interface to form yttrium oxide. The present work suggested that (i) alloying with Y elements and (ii) reducing the chemical/microstructural inhomogeneity of the bulk alloy may be beneficial in developing oxidation-resistant alloys.

Acknowledgments

The work was financially supported by the Natural Science Foundation of Hunan Province (Grant No. 2023JJ30673).

Conflicts of Interest

The authors declare no conflicts of interest.

Data Availability Statement

Data that support the findings of this study are available from the corresponding author upon reasonable request.

References

1. F. Czerwinski, "The Reactive Element Effect on High-Temperature Oxidation of Magnesium," *International Materials Reviews* 60 (2015): 264–296.

2. J. Song, J. She, D. Chen, and F. Pan, "Latest Research Advances on Magnesium and Magnesium Alloys Worldwide," *Journal of Magnesium & Alloys* 8 (2020): 1–41.

3. H. R. Bakhsheshi-Rad, E. Hamzah, M. Medraj, et al., "Effect of Heat Treatment on the Microstructure and Corrosion Behaviour of Mg–Zn Alloys," *Materials & Corrosion* 65 (2014): 999–1006.

4. H. R. Bakhsheshi-Rad, E. Hamzah, A. Fereidouni-Lotfabadi, et al., "Microstructure and Bio-Corrosion Behavior of Mg–Zn and Mg–Zn–Ca Alloys for Biomedical Applications," *Materials and Corrosion* 65 (2014): 1178–1187.

5. X. J. Wang, D. K. Xu, R. Z. Wu, et al., "What Is Going on in Magnesium Alloys," *Journal of Materials Science & Technology* 34 (2018): 245–247.

6. Q. Tan, A. Atrens, N. Mo, and M.-X. Zhang, "Oxidation of Magnesium Alloys at Elevated Temperatures in Air: A Review," *Corrosion Science* 112 (2016): 734–759.

7. F. Czerwinski, "Oxidation Characteristics of Magnesium Alloys," *JOM* 64 (2012): 1477–1483.

8. F. Czerwinski, "Role of Surface Reactivity in Processing and Performance of Magnesium Alloys," *Materials Science Forum* 828–829 (2015): 401–406.

9. X. M. Wang, X. Q. Zeng, G. S. Wu, and S. S. Yao, "Yttrium Ion Implantation on the Surface Properties of Magnesium," *Applied Surface Science* 253 (2006): 2437–2442.

10. J. F. Fan, G. C. Yang, Y. H. Zhou, Y. H. Wei, and B. S. Xu, "Selective Oxidation and the Third-Element Effect on the Oxidation of Mg-Y Alloys at High Temperatures," *Metallurgical and Materials Transactions A* 40 (2009): 2184–2189.

11. P. Lin, H. Zhou, W. Li, W. Li, S. Zhao, and J. Su, "Effect of Yttrium Addition on the Oxide Scale of AM50 Magnesium Alloy," *Corrosion Science* 51 (2009): 1128–1133.

12. Z. Ning, W. Liang, F. Cao, and J. Sun, "The Effect of Y on the Oxidation of Mg-Zn-Zr Alloys," *International Journal of Modern Physics B* 23 (2009): 796–801.

13. C. Cheng, Q. Lan, A. Wang, Q. Le, F. Yang, and X. Li, "Effect of Ca Additions on Ignition Temperature and Multi-Stage Oxidation Behavior of AZ80," *Metals* 8 (2018): 766.

14. X. Yu, J. Li, B. Jiang, C. Yang, J. Yang, and S. Chen, "Effect of Ce Addition on the High-Temperature Oxidation Resistance of Mg–Gd Alloys," *Materials and Corrosion* 73 (2022): 1383–1392.

15. B. A. Pint, "Limitations on the Use of Surface Doping for Improving High-Temperature Oxidation Resistance," *MRS Bulletin* 19 (1994): 26–30.

16. S.-M. Baek, H. J. Kim, H. Y. Jeong, et al., "Effect of Alloyed Ca on the Microstructure and Corrosion Properties of Extruded AZ61 Mg Alloy," *Corrosion Science* 112 (2016): 44–53.

17. Q. Tan, N. Mo, C. L. Lin, et al., "Improved Oxidation Resistance of Mg-9Al-1Zn Alloy Microalloyed With 60 Wt ppm Be Attributed to the Formation of a More Protective (Mg,Be)O Surface Oxide," *Corrosion Science* 132 (2018): 272–283.

18. D. S. Aydin, Z. Bayindir, M. Hoseini, and M. O. Pekguleryuz, "The High Temperature Oxidation and Ignition Behavior of Mg–Nd Alloys Part I: The Oxidation of Dilute Alloys," *Journal of Alloys and Compounds* 569 (2013): 35–44.

19. P. Lin, H. Zhou, W. Li, W. Li, N. Sun, and R. Yang, "Interactive Effect of Cerium and Aluminum on the Ignition Point and the Oxidation Resistance of Magnesium Alloy," *Corrosion Science* 50 (2008): 2669–2675.

20. S. Tekumalla and M. Gupta, "An Insight Into Ignition Factors and Mechanisms of Magnesium Based Materials: A Review," *Materials & Design* 113 (2017): 84–98.

21. X. M. Wang, X. Q. Zeng, Y. Zhou, G. S. Wu, S. S. Yao, and Y. J. Lai, "Early Oxidation Behaviors of Mg–Y Alloys at High Temperatures," *Journal of Alloys and Compounds* 460 (2008): 368–374.

22. X. Yu, B. Jiang, J. He, B. Liu, and F. Pan, "Oxidation Resistance of Mg-Y Alloys at Elevated Temperatures and the Protection Performance of the Oxide Films," *Journal of Alloys and Compounds* 749 (2018): 1054–1062.

23. X. Yu, B. Jiang, H. Yang, Q. Yang, X. Xia, and F. Pan, "High Temperature Oxidation Behavior of Mg-Y-Sn, Mg-Y, Mg-Sn Alloys and Its Effect on Corrosion Property," *Applied Surface Science* 353 (2015): 1013–1022.

24. J. J. Wu, Y. Yuan, L. Yang, et al., "The Oxidation Behavior of Mg-Er Binary Alloys at 500°C," *Corrosion Science* 195 (2022): 109961.

25. J. J. Wu, Y. Yuan, T. Chen, et al., "The Oxidation Behavior and Reaction Thermodynamics and Kinetics of the Mg-X (X = Ca/Gd/Y) Binary Alloys," *Corrosion Science* 225 (2023): 111609.

26. S. Tekumalla, C. Yang, S. Seetharaman, et al., "Enhancing Overall Static/Dynamic/Damping/Ignition Response of Magnesium Through the Addition of Lower Amounts (< 2%) of Yttrium," *Journal of Alloys and Compounds* 689 (2016): 350–358.

27. J. F. Fan, S. L. Cheng, H. Xie, et al., "Surface Oxidation Behavior of Mg-Y-Ce Alloys at High Temperature," *Metallurgical and Materials Transactions A* 36a (2005): 235–239.

28. X. M. Wang, W. D. Wu, Y. J. Tang, X. Q. Zeng, and S. S. Yao. "Early High Temperature Oxidation Behaviors of Mg-10Gd-3Y Alloys," *Journal of Alloys and Compounds* 474 (2009): 499.

29. G. Greczynski and L. Hultman, "C1s Peak of Adventitious Carbon Aligns to the Vacuum Level: Dire Consequences for Material's Bonding Assignment by Photoelectron Spectroscopy," *Chemphyschem* 18 (2017): 1507–1512.

30. S. K. Das, Y. B. Kang, T. Ha, and I. H. Jung, "Thermodynamic Modeling and Diffusion Kinetic Experiments of Binary Mg–Gd and Mg–Y Systems," *Acta Materialia* 71 (2014): 164–175.

31. O. Norman Carlson, F. A. Schmidt, and R. L. Wells, *A Study of the High-Temperature Air Oxidation of Yttrium Metal* (Chișinău: Generic, 1960).

32. X. Chen, C. Liu, S. Jiang, Z. Chen, and Y. Wan, "Effect of Yttrium on Nanocrystallization of Magnesium Alloys During Cold Rotary Swaging," *Materials Characterization* 184 (2022): 111696.

33. L. P. Bonfrisco and M. Frary, "Effects of Crystallographic Orientation on the Early Stages of Oxidation in Nickel and Chromium," *Journal of Materials Science* 45 (2010): 1663–1671.

34. L. Nguyen, T. Hashimoto, D. N. Zakharov, et al., "Atomic-Scale Insights Into the Oxidation of Aluminum," *ACS Applied Materials & Interfaces* 10 (2018): 2230–2235.

35. P. A. Tellex and J. R. Waldron, "Reflectance of Magnesium Oxide," *Journal of the Optical Society of America* 45 (1955): 19.

36. W. E. Knowles Middleton and C. L. Sanders, "The Absolute Spectral Diffuse Reflectance of Magnesium Oxide," *Journal of the Optical Society of America* 41 (1951): 419.

37. G. Steinborn, G. Tzschichholz, J. Guenster, M. H. Keller, and J. Manara, "Porous TiO_2-Y_2O_3 Ceramics With Specific Infrared-Optical Properties," *Journal of Ceramic Science & Technology* 2 (2011): 183–190.

38. M. Zhang, "Morphology and Crystallography of $Mg_{24}Y_5$ Precipitate in Mg–Y Alloy," *Scripta Materialia* 48 (2003): 379–384.

39. R. Reichl and K. H. Gaukler, "An Investigation of Air-Grown Yttrium Oxide and Experimental Determination of the Sputtering Yield and the Inelastic Mean Free Path," *Applied Surface Science* 26 (1986): 196–210.

40. B. V. Crist, "XPS in Industry—Problems With Binding Energies in Journals and Binding Energy Databases," *Journal of Electron Spectroscopy and Related Phenomena* 231 (2019): 75–87.

41. E.-M. Köck, M. Kogler, T. Bielz, B. Klötzer, and S. Penner, "In Situ FT-IR Spectroscopic Study of CO2and CO Adsorption on Y_2O_3, ZrO_2, and Yttria-Stabilized ZrO_2," *The Journal of Physical Chemistry C* 117 (2013): 17666–17673.

42. U. Burghaus, "Surface Chemistry of CO_2 – Adsorption of Carbon Dioxide on Clean Surfaces at Ultrahigh Vacuum," *Progress in Surface Science* 89 (2014): 161–217.

43. G. Greczynski and L. Hultman, "Towards Reliable X-Ray Photoelectron Spectroscopy: Sputter-Damage Effects in Transition Metal Borides, Carbides, Nitrides, and Oxides," *Applied Surface Science* 542 (2021): 148599.

44. K. Ando, Y. Oishi, H. Hase, and K. Kitazawa, "Oxygen Self-Diffusion in Single-Crystal Y_2O_3," *Journal of the American Ceramic Society* 66 (1983): C222–C223.

45. A. E. Hughes, A. Atkinson, and A. T. Chadwick, "Short-Circuit Diffusion Processes in Oxidation Films," *MRS Proceedings* 24 (1983): 27.